

Quantum Path Computing and Communications with Fourier Optics

Burhan Gulbahar

Abstract

Multi-plane diffraction (MPD) systems with classical sources and conventional intensity detection are recently proposed for scalable quantum computing (QC) and communications (QComm) with time domain entanglement resources and by exploiting the energy efficient interference of exponentially increasing number of propagation paths. MPD provides unique advantages for the challenges of scalability of qubits and complex set-ups including single photon generation and detection mechanisms in state-of-the-art linear optics implementations. However, MPD based QC architectures denoted by quantum path computing (QPC) are theoretically modeled for only electron based system set-up with Gaussian sources while proposed classical communication architectures are defined for free space propagation without modeling for arbitrary Fourier optical set-ups being mathematically equivalent to linear canonical transforms (LCTs). In this article, MPD architectures are defined, theoretically modeled and numerically analyzed for Fourier optics with arbitrary LCTs between diffraction planes while utilizing both Gaussian and Hermite-Gaussian laser modes. Photonic MPD proposes QC and QComm based on the mature science of Fourier optics significantly developed since the last century with globally available resources for fast and wide spread development of the proposed design. It promises the simplest linear optical system with important QC applications while promising novel resources for classical and quantum communications.

Index Terms

Quantum path computing, Fourier optics, multi-plane diffraction, linear canonical transform, fractional Fourier transform.

Burhan Gulbahar is with the Department of Electrical and Electronics Engineering and Applied Research Center of Technology Products, Ozyegin University, 34794 Istanbul, Turkey, e-mail: burhan.gulbahar@ozyegin.edu.tr.

I. INTRODUCTION

Multi-plane diffraction (MPD) based quantum computing (QC) and communication (QComm) systems are recently introduced in [1]–[3] as the simplest and scalable linear optical architectures with significantly important advantages combining the utilization of the classical sources, simplicity of the set-up composed of only planes with diffraction slits and detection with conventional intensity photodetectors. MPD proposes a promising alternative architecture coping with the fundamental challenges of scalability of multi-photon entanglement resources and the requirements of single photon sources and detection mechanisms in conventional linear optical QC [4]–[7]. Exponentially increasing number of propagation paths as a unique form of non-Gaussian transformation of the classical source provides QC, i.e., denoted as quantum path computing (QPC) in [1], and time domain entanglement resources for QComm by utilizing tensor product Hilbert spaces in time domain [2]. Besides that, diffractive and phase space optics are also getting attention with periodic single plane diffraction (SPD) structures for implementing quantum logic gates using quantum Talbot effect [8], to test D -dimensional (qudit) Bell inequality with free space entangled quantum carpets [9], and evaluating of entanglement over the entire transverse field distribution of the photons [10] while without any discussion regarding the MPD based advantages. MPD not only promises the solutions of important number theoretical problems such as partial sum of Riemann theta function and Diophantine approximation as a QC application [1] but also brings a novel form of quantum spatial modulation (QSM) exploiting the quantum properties of light including large Hilbert space and unique interference pattern in [3] for classical optical communications. However, MPD interference pattern is formulated for electron based set-up and Gaussian sources in [1], [2] while defined only for free space propagation (FSP) of light in [3] without generalizing to arbitrary set-ups of Fourier optics, i.e., first order centered optical or quadratic-phase systems including arbitrary sections of free space, thin lenses, graded index media and spatial filters [11]. Quadratic-phase systems are mathematically characterized as linear canonical transforms (LCTs) as discussed in Section III [12].

In this article, MPD set-up is defined, theoretically modeled and numerically analyzed for Fourier optical systems with arbitrary LCTs between diffraction planes. The quantum nature of Fourier optics is discussed based on the recent experimental [13] and theoretical [14] studies verifying the validity of Fresnel diffraction formulation for quantum optical propagation. LCTs are linear integral transforms including the Fresnel and fractional Fourier transform (FRFT),

scaling, chirp multiplication and some other operations as special cases while being equivalent to spatial distribution of light in phase-space optics for quadratic-phase systems [11]. Classical monochromatic light sources of both Gaussian and Hermite-Gaussian (HG) beams are utilized compatible with the standard laser sources within the paraxial approximation [15]. LCT based design which provides more flexibility is numerically compared with FSP in terms of improvement on the detection efficiency, i.e., probability of the detection or intensity at the sensor plane, and the interference complexity defined with the magnitudes of the interfering paths and negative volume of Wigner distribution function [1], [16]. It is observed that photonic MPD with Gaussian sources results in unique mathematical forms of intensity distribution on the sensor plane in (18) which are promising to be exploited for the solutions of the partial sum of Riemann theta function [17]–[20], period finding [21] and Diophantine approximation [22] similar to the algorithms and methods in [1] but with much more design flexibility due to LCTs, diversity of the tools and maturity in Fourier optics. Furthermore, HG sources result in different forms in (22) and (24) while closely related to the standard Riemann theta form and requiring future studies to exploit for the solutions of numerical problems in various scientific disciplines.

Proposed theoretical modeling and system design with widely available optical components, e.g., thin lenses, free space and diffraction planes as a form of spatial filtering, provide a unique opportunity to exploit conventional Fourier optics for QC and QComm purposes. The large amount of theoretical and experimental maturity in Fourier optics since the last century is combined with MPD based system design to realize scalable and low complexity QC, QComm and classical communications systems with important capabilities and global resources for efficient implementation and development.

The remainder of the paper is organized as follows. In Section II, MPD based design and advantages for QC and QComm are briefly reviewed. In Section III, quantum nature of Fourier optics and modeling of light propagation are discussed. Then, in Section IV, theoretical modeling of MPD with arbitrary LCT set-ups is presented for Gaussian and HG sources. The negativity of Wigner distribution function and the path magnitudes are discussed in Section V while numerical analysis is provided in Section VI. Finally, in Sections VII and VIII, open issues and conclusions are given.

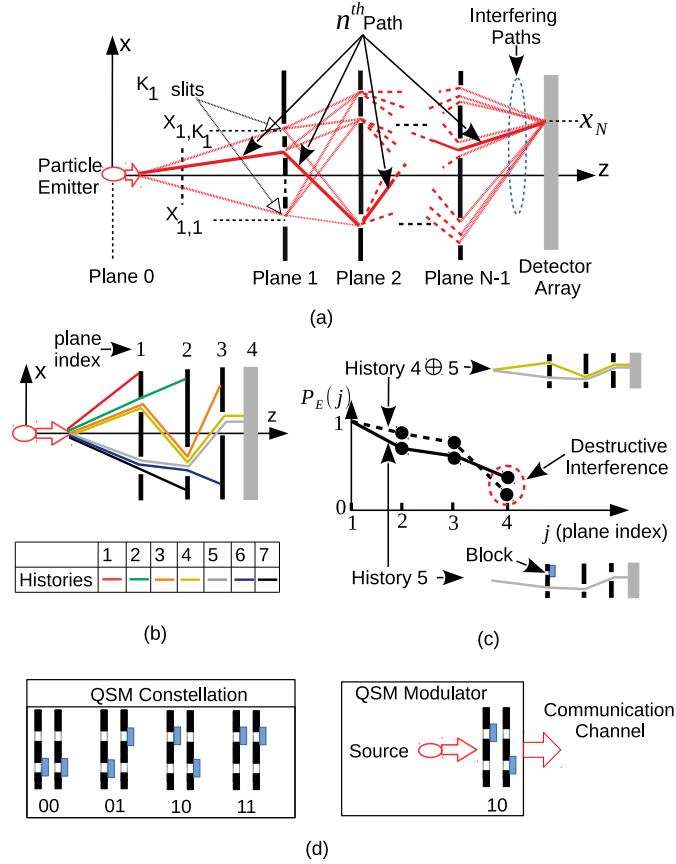


Fig. 1. (a) MPD set-up composed of $N - 1$ diffraction planes, FSP between the planes and a single sensor plane on which exponentially increasing number of propagation paths interfere [1]. (b) An example showing seven different consistent or entangled histories including diffraction and consecutive measurement operations on the planes [2] and (c) a scenario of interference in time where the probability of the particle to be diffracted through the first and the second planes, i.e., $P_E(2)$ and $P_E(3)$, increases with the superposition of the paths or histories with indices 4 and 5 while decreasing through the third plane, i.e., $P_E(4)$ on the fourth (detector) plane, due to the destructive interference between the two paths [2]. (d) The constellation diagram and QSM block diagram where blocking varying combinations of slits results in the superposition of varying paths which are utilized as different QSM symbols [3].

II. QUANTUM PATH COMPUTING AND COMMUNICATIONS WITH CLASSICAL SOURCES

MPD set-up is introduced and the applications for QC, QComm and classical communications proposed in [1]–[3] are briefly reviewed in the following while emphasizing the QPC capability. The set-up is composed of $N-1$ diffraction planes with K_j slits on each plane for $j \in [1, N-1]$ and a single sensor plane indexed with N while the center of the slits is given by $X_{j,i}$ for $i \in [1, K_j]$ as shown in Fig. 1(a). Each slit is assumed to apply a spatial filtering of $\exp(- (x_j - X_{j,i})^2 / (2\tilde{\beta}_{j,i}^2))$ where $\tilde{\beta}_{j,i}$ determines the slit width. The wave function on j th plane is denoted with $\Psi_j(x_j)$

which is the wave form after diffraction through the previous planes, i.e., with the indices $k \in [1, j - 1]$, while before diffraction through the slits on j th plane. There is an exponentially increasing number of propagation paths through the slits until to the final sensor plane, i.e., $N_p \equiv \prod_{j=1}^{N-1} K_j$, while n th path includes the diffraction through a single slit on each plane with the corresponding wave function $\Psi_{j,n}(x_j)$ on j th plane. Assume that n th path passes through the slit indexed with $s_{n,j}$ on j th plane and define the path vectors $\vec{x}_{N-1,n}^T \equiv [X_{1,s_{n,1}} \ X_{2,s_{n,2}} \ \dots \ X_{N-1,s_{n,N-1}}]$ and $\vec{x}_{N-1,\vec{s}}^T \equiv [X_{1,s_1} \ X_{2,s_2} \ \dots \ X_{N-1,s_{N-1}}]$ where $\vec{s} \equiv [s_1 \ s_2 \ \dots \ s_{N-1}]$ and $(\cdot)^T$ is the transpose operation. The mapping between the path index n and slit index $s_{n,j}$ for the path is defined with the function $n = f_{s2n}(\vec{s})$ where $s_{n,j}$ is predefined for each n . Furthermore, $\vec{0}_k$ is the column vector of length k with all zeros and $\mathbf{0}_k$ is the square matrix of all zeros with the size $k \times k$. Similarly, rectangular matrices are shown with $\mathbf{0}_{k,l}$. In the rest of the article, a parameter B depending only on $\vec{\beta}_{N-1,n} \equiv [\beta_{1,s_{n,1}} \ \dots \ \beta_{N-1,s_{n,N-1}}]$ but not on $\vec{x}_{N-1,n}$ is denoted with $\widetilde{B}_{j,n}$ on each j th plane including \sim over the symbol. Therefore, if the slits are chosen with the same $\widetilde{\beta}_{j,n} = \beta_j$ specific to each plane, then $\widetilde{B}_{j,n}$ becomes independent of n and is converted to the notation B_j .

MPD set-up shown in Fig. 1(a) is utilized for QC denoted by QPC in [1] with exponentially increasing number of interfering paths as quantum resources. Consistent and entangled histories approaches are utilized in [2] to show Leggett-Garg inequality violation as the temporal analogue of Bell inequality requiring further studies to exploit the proposed time domain entanglement resources for practical QComm. An example including seven different histories of the propagation composed of diffraction through slits and measurements on the planes is shown in Fig. 1(b). A scenario showing the interference between different path histories is simulated in [2] as shown in Fig. 1(c) where two different set-ups are utilized. The first set-up is composed of two diffraction paths or histories indexed with 4 and 5. The second set-up includes only the path with the index 5 obtained by blocking the upper slit on the first plane. The constructive interference between the two paths allows an increase in the probability of the particle to be diffracted through the first two planes, i.e., the probability of $P_E(j)$ to be detected on the planes with the indices $j = 2$ and $j = 3$, compared with the fifth path alone while the destructive interference reduces the probability to be diffracted through the third plane as a counter-intuitive observation. Furthermore, a novel form of QSM is defined in [3] where opening and closing slits result in varying quantum superposition waveform message symbols at the transmitter which can be detected at the receiver as shown in Fig. 1(c). Interference of exponentially increasing number of paths is exploited which is not

possible in classical domain. As a result, the capability to theoretically characterize MPD with quantum Fourier optics provides future applications of QC, QComm, quantum information theory and classical communications by exploiting energy efficient combination of optical elements.

MPD set-up measurement on the sensor plane in [1], [2] generates a black-box (BB) function $f_{BB}[k]$ with the following special form to utilize in solutions of important and classically hard number theoretical problems:

$$f_{BB}[k] \equiv \left| \sum_{s_1=1}^{K_1} \dots \sum_{s_{N-1}=1}^{K_{N-1}} e^{(\tilde{A}_{\vec{s}} + \iota \tilde{B}_{\vec{s}})(k T_s)^2} \tilde{\Upsilon}_{\vec{s}} e^{\tilde{x}_{N-1, \vec{s}}^T \tilde{\mathbf{H}}_{\vec{s}} \tilde{x}_{N-1, \vec{s}}} e^{(\tilde{h}_{\vec{s}}^T \tilde{x}_{N-1, \vec{s}}) k T_s} \right|^2 \quad (1)$$

where $k \in \mathbb{Z}$, $T_s \in \mathbb{R}^+$ is a sampling interval, $\tilde{A}_{\vec{s}} \in \mathbb{R}^-$, $\tilde{B}_{\vec{s}} \in \mathbb{R}^+$ and $\tilde{\Upsilon}_{\vec{s}} \in \mathbb{C}$. The complex valued matrix $\tilde{\mathbf{H}}_{\vec{s}} \equiv \tilde{\mathbf{H}}_{R, \vec{s}} + \iota \tilde{\mathbf{H}}_{I, \vec{s}}$ and the vector $\tilde{h}_{\vec{s}} \equiv \tilde{c}_{\vec{s}} + \iota \tilde{d}_{\vec{s}}$ have the values depending on $\tilde{\beta}_{j,i}$ for $j \in [1, N-1]$ and $i \in [1, K_j]$ corresponding to the specific selection of slits in the path \vec{s} , inter-plane durations for the particle propagation, particle mass m (for electron based set-ups in [1], [2]), beam width σ_0 of the Gaussian source wave packet and Planck's constant \hbar . The calculation of (1) in an efficient manner is significantly hard while two different methods utilizing (1) for practical problems are introduced. Solution for the partial sum of Riemann theta or multi-dimensional theta function is the first application with importance in number theory and geometry [17]–[20]. The second method utilizes MPD with the phase $\tilde{d}_{\vec{s}}^T \tilde{x}_{N-1, \vec{s}}$ in $\exp(\tilde{h}_{\vec{s}}^T \tilde{x}_{N-1, \vec{s}} k T_s)$ for period finding [21] and the solution of specific instances of SDA problems [22].

QPC based on Fourier optics promises expanding the set of problems both with LCT based general system design and also the sources including HG beams. Furthermore, a discussion is included to utilize non-Gaussian slits with the proposed mathematical modeling in Section VII. Next, the propagation through Fourier optical systems based on Fresnel diffraction is modeled emphasizing the quantum nature of Fresnel diffraction and Fourier optics.

III. QUANTUM FOURIER OPTICS

In scalar diffraction theory, the first Rayleigh-Sommerfeld formula of the Huygens-Fresnel principle for the propagation of light on planar surfaces is described as follows by using the Green's theorem [23]:

$$U_I(P_1) = \frac{-1}{4\pi} \iint_{\Sigma} U \frac{\delta G_-}{\delta n} ds \quad (2)$$

where $U_I(P_1)$ is the wave amplitude at the point P_1 , U is the distribution on the planar screen where diffraction occurs, Σ denotes the integration over the slit including its multiplicative

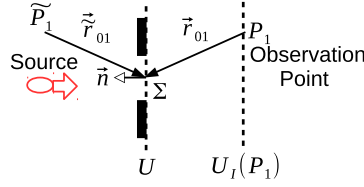


Fig. 2. Formulation set-up for first type of solution of Rayleigh-Sommerfeld diffraction through a slit Σ [23].

effects on the wave amplitude, $G_- \equiv \exp(i k r_{01}) / r_{01} - \exp(i k \tilde{r}_{01}) / \tilde{r}_{01}$ is the Green's function vanishing on the diffraction surface for the first type of solution of Rayleigh-Sommerfeld formula, $r_{01} \equiv |\vec{r}_0 - \vec{r}_1|$ and $k \equiv 2\pi / \lambda$ for the monochromatic light source of wavelength λ as shown in Fig. 2 [23]. Assuming that $r_{01} \gg \lambda$, the following approximation holds in rectangular coordinates:

$$U_I(P_1) \approx \iint_{\Sigma} U(x_0, y_0) K_{FS}(\vec{r}_1, \vec{r}_0) dx_0 dy_0 \quad (3)$$

where the kernel $K_{FS}(\vec{r}_1, \vec{r}_0)$ for FSP is defined as follows:

$$K_{FS}(\vec{r}_1, \vec{r}_0) \equiv \frac{1}{i\lambda} \frac{e^{i k r_{01}}}{r_{01}} \cos(\vec{n}, \vec{r}_{01}) \quad (4)$$

$$= \frac{z}{i\lambda} \frac{e^{i k r_{01}}}{r_{01}^2} \quad (5)$$

$$\approx \frac{e^{j k z}}{i\lambda z} e^{\frac{i k}{2z} ((x_1 - x_0)^2 + (y_0 - y_0)^2)} \quad (6)$$

where $r_{01} = \sqrt{z^2 + (x_1 - x_0)^2 + (y_0 - y_0)^2}$. The kernel for Fresnel diffraction integral is obtained by further approximation of r_{01} in the near-field for large z resulting in (6). This expression is the convolution integral conventionally used in phase-space optics for FSP [11].

Recently, scalar diffraction theory and Fresnel diffraction integral are discussed in [13] to be validly representing the evolution of light wave function modeled with the Hamiltonian of the quantized electromagnetic field $H = (\hat{p}^2 + \omega^2 \hat{q}^2) / 2$ as the Feynman's path integral (FPI) solution of the quantum mechanical harmonic oscillator (HO) [24]. Fresnel diffraction nature of the propagation is verified with experimental photon counting studies for single photons. The wave function amplitude of light field in one dimension (1D) on a plane $\Psi(x_0)$ is modeled to propagate into the amplitude $\Psi(x_1)$ on another plane (Eq. 16 in [13] transformed into a simpler form) with the following formulation:

$$\Psi(x_1) \approx \int_{-\infty}^{\infty} \Psi(x_0) K_{HO}(x_1, x_0) dx_0 \quad (7)$$

where the kernel based on HO is the following:

$$K_{HO}(x_1, x_0) \equiv \sqrt{\frac{m_\lambda}{2\pi i \hbar t_{01} \sin(\omega t)}} \exp\left(\frac{i m_\lambda (x_1^2 \cos(\omega t) - 2x_1 x_0 + x_0^2 \cos(\omega t))}{2\hbar t_{01} \sin(\omega t)}\right) \quad (8)$$

where c is the velocity of light, $\omega \equiv 2\pi c / \lambda$, $\omega t \neq n\pi$ for $n \in \mathbb{Z}$, t_{01} is the propagation duration between the planes and $m_\lambda \equiv \hbar k / c$ is the defined equivalent mass of photon propagation. In addition, the approximated FSP kernel in (6) is simply converted to the following in 1D:

$$K_{FS}(x_1, x_0) \approx e^{jkz} \sqrt{\frac{m_\lambda}{2\pi i \hbar t_{01}}} e^{\frac{i m_\lambda}{2\hbar t_{01}} (x_1 - x_0)^2} \quad (9)$$

The kernel for massive particles with the mass m such as an electron is expressed as follows [1], [24]:

$$K_{m,FS}(x_1, x_0) \approx \sqrt{\frac{m}{2\pi i \hbar t_{01}}} e^{\frac{i m}{2\hbar t_{01}} (x_1 - x_0)^2} \quad (10)$$

In other words, the formulation based on phase-space optics for photon and electron propagation wave amplitudes have the similar form in (9) and (10) except an overall phase factor. The form in (9) is utilized in [3] for defining QSM while targeting only classical communications.

On the other hand, both the kernels $K_{HO}(x_1, x_0)$ and $K_{FS}(x_1, x_0)$ are special cases of LCTs defined for quadratic-phase optics [11]. As a class of linear integral transforms, they include as special cases the Fresnel and fractional Fourier transform (FRFT), simple scaling, chirp multiplication and some other operations. Spatial distribution of light in phase-space optics for the class denoted by quadratic-phase systems is mathematically equivalent to LCTs (Chapters 3 and 8 in [11]). These optical systems include arbitrary combinations of the sections of free space in the Fresnel approximation, thin lenses and sections of quadratic graded-index media. In [13], FRFT nature of the kernel $K_{HO}(x_1, x_0)$ is shown both theoretically and experimentally while emphasizing the applicability of all the properties of Fourier analysis to quantum optics. In this article, propagation of the wave function is extended to the general case of LCTs providing flexibility to utilize arbitrary optical set-ups by enlarging the functional structures and number theoretical problems exploited in QPC. Furthermore, a better control is obtained for the energy flow of the light through the slits. The kernel of 1D quadratic-phase system or LCT is represented as follows:

$$K_{LCT}^{(a,b,c,d)}(x_1, x_0) \approx \sqrt{\frac{1}{b}} e^{-\frac{i\pi}{4}} e^{\frac{i\pi}{b}(d x_1^2 - 2x_1 x_0 + a x_0^2)} \quad (11)$$

In matrix notation, it is shown with the following unit-determinant matrix:

$$\mathbf{M}_{LCT} = \begin{bmatrix} a & b \\ c & d \end{bmatrix} \quad (12)$$

where $ad - bc = 1$ and the matrix for the composition of two consecutive systems represented by \mathbf{M}_1 and \mathbf{M}_2 is calculated by the multiplication $\mathbf{M}_2 \mathbf{M}_1$. The matrices for $K_{HO}(x_1, x_0)$ and $K_{FS}(x_1, x_0)$ are given as follows:

$$\mathbf{M}_{HO} = \begin{bmatrix} \cos(\omega t) & \frac{2\pi \hbar t_{01} \sin(\omega t)}{m_\lambda} \\ -\frac{m_\lambda \sin(\omega t)}{2\pi \hbar t_{01}} & \cos(\omega t) \end{bmatrix} \quad (13)$$

$$\mathbf{M}_{FS} = \begin{bmatrix} 1 & \frac{2\pi \hbar t_{01}}{m_\lambda} \\ 0 & 1 \end{bmatrix} \quad (14)$$

\mathbf{M}_{HO} has the same form with the propagation of light in quadratic graded-index media of having the refractive index distribution of $n^2(x) = n_0^2(1 - (x/\chi)^2)$ where n_0 and χ are the medium parameters. The parameter matrix of the propagation through the quadratic graded-index medium of length d_{gri} is given by the following [11]:

$$\mathbf{M}_{gri} = \begin{bmatrix} \cos(\alpha) & \lambda_\chi \sin(\alpha) \\ -\sin(\alpha)/\lambda_\chi & \cos(\alpha) \end{bmatrix} \quad (15)$$

where $\alpha = d_{gri}/\chi$. There is a FRFT relation between scaled versions of the input $\hat{f}(x)$ and output $\hat{g}(x)$ with FRFT order α as $\hat{g}(x) = e^{-i d_{gri}/(2\chi)} \lambda_\chi^{-1/4} f_a(x/\sqrt{\lambda_\chi})$ where $f(x) \equiv \lambda_\chi^{1/4} \hat{f}(x\sqrt{\lambda_\chi})$ and $f_a(x)$ denotes the a th order FRFT of $f(x)$. FRFT operation of order α is represented with the parameter matrix of $a = d = \cos(\alpha)$ and $b = \sin(\alpha)$. As a result, \mathbf{M}_{HO} represents a FRFT relation between the input and output scaled with the parameter $\sqrt{\lambda_\chi}$ where the parameters are $\alpha = \omega t$ and $\lambda_\chi \equiv 2\pi \hbar t_{01}/m_\lambda$ while as a special case of LCTs. Next, MPD modeling is proposed for Fresnel diffraction and arbitrary LCT based optical systems by utilizing the proposed kernels.

IV. MULTI-PLANE DIFFRACTION WITH QUANTUM FOURIER OPTICAL SYSTEMS

The set-up in Fig. 1(a) defined with FSP and electron based theoretical formulation is extended to optical systems of LCT as shown in Fig. 3. An arbitrary LCT with the matrix parameters $\{a_{j,j+1}, b_{j,j+1}, c_{j,j+1}, d_{j,j+1}\}$ is implemented in phase-space optics by consecutive applications of FSP of length $L_{a,j,j+1}$, then thin lens of focal length $f_{j,j+1}$, and another FSP of length $L_{b,j,j+1}$ [12]. LCT matrix \mathbf{M}_{LCT} is calculated as follows:

$$\mathbf{M}_{LCT} \equiv \begin{bmatrix} 1 & \frac{2\pi \hbar \tau_{b,j}^*}{m_\lambda} \\ 0 & 1 \end{bmatrix} \begin{bmatrix} 1 & 0 \\ -\frac{1}{\lambda f_{j,j+1}} & 1 \end{bmatrix} \begin{bmatrix} 1 & \frac{2\pi \hbar \tau_{a,j}^*}{m_\lambda} \\ 0 & 1 \end{bmatrix} \quad (16)$$

where $\tau_{a,j}^* \equiv L_{a,j,j+1}/c$ and $\tau_{b,j}^* \equiv L_{b,j,j+1}/c$, and the middle matrix is for the effect of thin lens [11]. FRFT with scaling is a special case of LCT as discussed in Section III. Therefore, FSP,

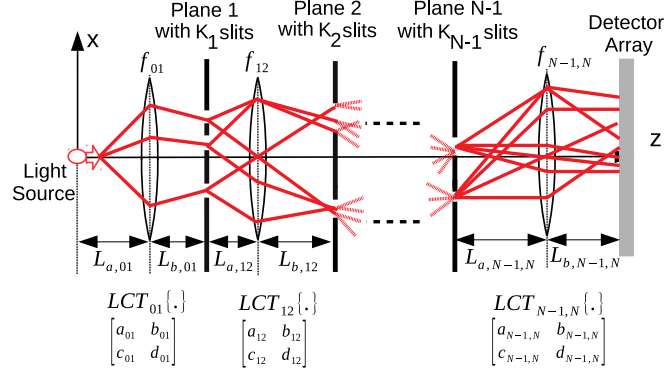


Fig. 3. Photonic QPC architecture composed of classical light source, MPD set-up composed of $N-1$ diffraction planes with K_j slits on j th plane, general LCT phase-space optics represented with the matrix elements $LCT_{j,j+1}$ between the planes indexed with j and $j+1$, and a single sensor plane on which exponentially increasing number of propagation paths interfere. Each $LCT_{j,j+1}$ is implemented with sections of FSP for the lengths of $L_{a,j,j+1}$ and $L_{b,j,j+1}$, and a thin lens of focal length $f_{j,j+1}$ between them.

FRFT and arbitrary LCT based QPC set-ups are implemented with the universal configuration in Fig. 3.

A. Fresnel Diffraction and FRFT with Gaussian Sources

It is assumed that the optical system between the planes results in the kernels defined in (6) and (8) based on Fresnel diffraction integral for free space and FRFT based propagation denoting graded-index media propagation or HO solution, respectively. It is assumed that the source distribution has a Gaussian form of $\Psi_0(x_0) = \exp(-x_0^2 / (2\sigma_0^2)) / \sqrt{\sigma_0} \sqrt{\pi}$ while HG waveforms as eigenfunctions of FRFTs [11] are considered for the general case of LCTs in Section IV-B2.

The kernel $K_{FS}(x_1, x_0)$ has the same form with $K_{e,FS}(x_1, x_0)$ used for QPC modeling in [1] by replacing the electron mass m with the photon equivalent mass m_λ . Therefore, the same formulations are utilized for both the final wave function and problem solving capabilities. In addition, iterative integration with $K_{HO}(x_1, x_0)$ results in the final intensity distribution of MPD with the same form of $K_{FS}(x_1, x_0)$ while with different iteration parameters as shown in Table II in Appendix D.

The wave function for n th path on the sensor plane for the general case of non-uniform slit

widths is given by the following by using the iterative formulation:

$$\Psi_{N,n}^G(x_N) = \chi_0 \left(\prod_{j=1}^{N-1} \chi_{j,n} \right) e^{(\tilde{A}_{N-1,n} + i \tilde{B}_{N-1,n}) x_N^2} e^{(C_{N-1,n} + i D_{N-1,n}) x_N} \quad (17)$$

It is further simplified by extraction of $\tilde{x}_{N-1,n}$ dependent parts and summing the contributions from each path as follows:

$$\Psi_N^G(x_N) = \sum_{n=0}^{N_p-1} \tilde{\Upsilon}_{N,n}^G e^{\tilde{x}_{N-1,n}^T} \tilde{\mathbf{H}}_{N-1,n}^{HO/G} \tilde{x}_{N-1,n} e^{(\tilde{A}_{N-1,n} + i \tilde{B}_{N-1,n}) x_N^2} e^{(\tilde{h}_{N-1,n}^T \tilde{x}_{N-1,n}) x_N} \quad (18)$$

where $\tilde{\Upsilon}_{N,n}^G \equiv \chi_0 \left(\prod_{j=1}^{N-1} \sqrt{\tilde{\xi}_{j,n}} \right)$, and the complex vector $\tilde{h}_{N-1,n}$ and the matrix $\tilde{\mathbf{H}}_{N-1,n}^{HO/G}$ are defined in Appendix A while having simpler structures compared with the formulation for electron based FSP set-up in [1]. The corresponding iteration parameters are given in Table II in Appendix D.

We have not included the effects of special forms of $K_{HO}(x_{j+1}, x_j)$ with $\omega t_{j,j+1} = k\pi$ for $k \in \mathbb{Z}$ since the result is $\Psi_{j+1}(x_{j+1}) \equiv \Psi_j(\pm x_{j+1})$ (inserting $\pm x_{j+1}$ into $\Psi_j(x_j)$) [11]. This case can be simply realized by assuming that spatial filtering operations of the slits on j th and $(j+1)$ th planes are combined on a single plane by also noting that whether the wave function is reversed or not. For example, multiple inter-plane propagation intervals can result in multiple reversals with the overall effect of the identity and combined spatial filtering of Gaussian slits.

B. Arbitrary Linear Canonical Transforming Optical Systems

1) *Gaussian Sources*: The resulting final intensity of MPD propagation for the case of $K_{LCT}^{(a,b,c,d)}$ ($b_{j,j+1} \neq 0$) with Gaussian sources has the same form with K_{HO} while with different iteration parameters in Table II in Appendix D and replacing $\tilde{\mathbf{H}}_{N-1,n}^{HO/G}$ with $\tilde{\mathbf{H}}_{N-1,n}^{LCT/G}$. Therefore, all the derivations utilized in Section IV-A including the explicit forms of the wave function are applicable. We have not included $K_{LCT}^{(a_{j,j+1}, b_{j,j+1}, c_{j,j+1}, d_{j,j+1})}$ with $b_{j,j+1} = 0$ for simplicity. Two simple cases are scaling with $d_{j,j+1} = 1/a_{j,j+1}$ resulting in $\Psi_{j+1}(x_{j+1}) \equiv (1 / \sqrt{a_{j,j+1}}) \Psi_j(x_{j+1} / a_{j,j+1})$ and chirp multiplication with $a_{j,j+1} = d_{j,j+1} = 1$ resulting in $\Psi_{j+1}(x_{j+1}) \equiv \exp(i\pi c x_{j+1}^2) \Psi_j(x_{j+1})$ [11]. These cases further improve the flexibility of the LCT system to realize the desired transformation on the wave function.

2) *Hermite-Gaussian Sources*: If the source is chosen as the standard HG waveform of $\Psi_0(x_0) = (2^{1/4} / \sqrt{W_0 2^l l!}) \exp(-\pi x_0^2 / W_0^2) H_l(\sqrt{2\pi} x_0 / W_0)$ for $K_{LCT}^{(a_{j,j+1}, b_{j,j+1}, c_{j,j+1}, d_{j,j+1})}$ ($b_{j,j+1} \neq 0$) where $H_l(x) \equiv (-1)^l e^{x^2} d^l e^{-x^2} / dx^l$ is the l th order Hermite polynomial [11], [25], then

$\Psi_{N,n}(x_N)$ for n th path is obtained as follows by using the integral equality of HG functions in Appendix B:

$$\Psi_{N,n}^{HG}(x_N) = \chi_{01} \left(\prod_{j=1}^{N-1} \chi_{j,j+1,n} \right) e^{\tilde{u}_{N-1,N,n} x_N^2} e^{v_{N-1,N,n} x_N} H_l(\tilde{g}_{N-1,N,n} x_N + h_{N-1,N,n}) \quad (19)$$

where the parameters χ_{01} , $\chi_{j,j+1,n}$, $\tilde{u}_{j,j+1,n}$, $v_{j,j+1,n}$, $\tilde{g}_{j,j+1,n}$ and $h_{j,j+1,n}$ obtained in an iterative manner for $j \in [1, N-1]$ are calculated with simple algebra for n th path and shown in Table III in Appendix D. Simple algebraic manipulations of (19) to extract $\tilde{x}_{N-1,n}$ dependent parts result in the following simplification:

$$\begin{aligned} \Psi_{N,n}^{HG}(x_N) &= \chi_{01} \left(\prod_{j=1}^{N-1} \tilde{\chi}_{a,j,j+1,n} \right) e^{\frac{-i\pi(N-2)}{4}} e^{\tilde{\gamma}_{N-1,n}^T \tilde{\mathbf{H}}_{N-1,n}^{LCT/HG} \tilde{x}_{N-1,n}} \\ &\times e^{(\tilde{\gamma}_{N-1,n}^T \tilde{x}_{N-1,n}) x_N} e^{\tilde{u}_{N-1,N,n} x_N^2} H_l(\tilde{g}_{N-1,N,n} x_N + \tilde{\eta}_{N-1,n}^T \tilde{x}_{N-1,n}) \end{aligned} \quad (20)$$

where $\tilde{\chi}_{a,j,j+1,n}$ for $j \in [1, N-1]$ is defined in Table III in Appendix D, the vectors $\tilde{\gamma}_{N-1,n}$ and $\tilde{\eta}_{N-1,n}$, and the matrix $\tilde{\mathbf{H}}_{N-1,n}^{LCT/HG}$ are defined in Appendix C. It is observed in (20) that each different path results in a different shift on Hermite polynomial determined with $\tilde{\eta}_{N-1,n}^T \tilde{x}_{N-1,n}$ even for the uniform β_j for each slit on j th plane. As a result, the final intensity distribution on the sensor plane denoted with $\Psi_N^{HG}(x_N)$ for the general case of non-uniform slit widths defined with $\tilde{\beta}_{j,n}$ for $j \in [1, N-1]$ and $n \in [0, N_p-1]$ is given by the following:

$$\begin{aligned} \Psi_N^{HG}(x_N) &= \sum_{n=0}^{N_p-1} \Psi_{N,n}^{HG}(x_N) \\ &= \sum_{n=0}^{N_p-1} \tilde{\gamma}_{N,n}^{HG} e^{\tilde{\gamma}_{N-1,n}^T \tilde{\mathbf{H}}_{N-1,n}^{LCT/HG} \tilde{x}_{N-1,n}} e^{\tilde{u}_{N-1,N,n} x_N^2} e^{(\tilde{\gamma}_{N-1,n}^T \tilde{x}_{N-1,n}) x_N} \\ &\quad \times H_l(\tilde{g}_{N-1,N,n} x_N + \tilde{\eta}_{N-1,n}^T \tilde{x}_{N-1,n}) \end{aligned} \quad (21)$$

where $\tilde{\gamma}_{N,n}^{HG} \equiv \chi_{01} \left(\prod_{j=1}^{N-1} \tilde{\chi}_{a,j,j+1,n} \right) e^{-i\pi(N-2)/4}$ and similarity to the form in (18) except multiplicative Hermite polynomial for each n th path. The complexity of calculating the Gaussian form in (18) is classically hard as thoroughly discussed in [1] which requires to compute a special form of partial sum of Riemann theta function while the complex vector $\tilde{h}_{N-1,n}$ and the matrix $\tilde{\mathbf{H}}_{N-1,n}^{HO/G}$ varying for each path making it much harder compared with the computation of conventional partial sum of Riemann theta function. Therefore, the complexity characterization of computing $\Psi_N^{HG}(x_N)$ is an open issue while it is expected to be significantly hard since each summation term depends on path index n with varying vector and matrix parameters while also including a product term of Hermite polynomial for each path making it harder.

If the uniform slit width case is chosen and the path independent variables are denoted with $\tilde{\Upsilon}_{N,n}^{HG} = \Upsilon_N^{HG}$, $\tilde{\chi}_{a,j,j+1,n} = \chi_{a,j,j+1}$, $\tilde{\mathbf{H}}_{N-1,n}^{LCT/HG} = \mathbf{H}_{N-1}^{LCT/HG}$, $\tilde{\gamma}_{N-1,n} = \tilde{\gamma}_{N-1}$, $\tilde{u}_{N-1,N,n} = u_{N-1,N}$, $\tilde{g}_{N-1,N,n} = g_{N-1,N}$, $\tilde{\eta}_{N-1,n} = \tilde{\eta}_{N-1}$, then (22) is transformed into the following:

$$\Upsilon_N^{HG} e^{u_{N-1,N} x_N^2} \sum_{n=0}^{N_p-1} e^{\tilde{x}_{N-1,n}^T \mathbf{H}_{N-1}^{LCT/HG} \tilde{x}_{N-1,n}} e^{(\tilde{\gamma}_{N-1}^T \tilde{x}_{N-1,n}) x_N} H_l(g_{N-1,N} x_N + \tilde{\eta}_{N-1}^T \tilde{x}_{N-1,n}) \quad (23)$$

It is further simplified as follows by using the useful identity $H_l(x + y) = (H + 2y)^l$ in [26] where $H^k \equiv H_k(x)$:

$$\Psi_N^{HG,U}(x_N) = \Upsilon_N^{HG} e^{u_{N-1,N} x_N^2} \sum_{n=0}^{N_p-1} e^{(\tilde{\gamma}_{N-1}^T \tilde{x}_{N-1,n}) x_N} e^{\tilde{x}_{N-1,n}^T \mathbf{H}_{N-1}^{LCT/HG} \tilde{x}_{N-1,n}} (H^*(x_N) + 2\tilde{\eta}_{N-1}^T \tilde{x}_{N-1,n})^l \quad (24)$$

where $(H^*(x_N))^k \equiv H_k(g_{N-1,N} x_N)$. The computational complexity of calculating $\Psi_N^{HG,U}(x_N)$ is similarly expected to be significantly hard since the mathematical form is more complicated compared with the partial sum of Riemann theta function.

The set-up parameters including the slits, lenses and inter-plane distances are required to be tuned in order to obtain the desired vectors $\tilde{h}_{N-1,n}$, $\tilde{\gamma}_{N-1,n}$, $\tilde{\eta}_{N-1,n}$ and matrices $\tilde{\mathbf{H}}_{N-1,n}^{HO/G}$, $\tilde{\mathbf{H}}_{N-1,n}^{LCT/G}$ and $\tilde{\mathbf{H}}_{N-1,n}^{LCT/HG}$ in (18), (22) and (24) for the target number theoretical problems. Next, Wigner distribution is defined where its negative volume is regarded as an indicator of non-classicality.

V. WIGNER DISTRIBUTION, NEGATIVITY AND PATH MAGNITUDES

The momentum domain wave function $\Psi_{p,j}(p_j)$ is defined as Fourier transform of spatial representation of wave function $\Psi_j(x_j)$ on j th plane as follows:

$$\Psi_{p,j}(p_j) = \frac{1}{\sqrt{2\pi\hbar}} \int dx_j \Psi_j(x_j) \exp(-i x_j p / \hbar) \quad (25)$$

The distribution of energy through space-momentum phase-space is described by Wigner distribution function defined as follows [1], [16]:

$$W_j(x_j, p_j) = \frac{1}{\pi\hbar} \int dy \Psi_j(x_j - y) \Psi_j^*(x_j + y) e^{\frac{i2p_j y}{\hbar}} \quad (26)$$

The negative volume of Wigner function defined in [16] and utilized in [1] to describe the increasing non-classicality or time-domain entanglement resources in [2] is described as $V_j \equiv (\int \int |W_j(x_j, p_j)| dx_j dp_j - 1) / 2$. On the other hand, the probability of the particle to be detected on j th plane, i.e., to be diffracted through $(j - 1)$ th plane, is computed as follows:

$$P_E(j) \equiv \int dx_j |\Psi_j(x_j)|^2 \quad (27)$$

TABLE I
MPD OPTICAL SET-UP PARAMETERS

ID	Property	Value
N, K_1, K_2	The number of planes and slits	3, 11, 27
σ_0, W_0, l	Gaussian & HG beam-width and order	20 μm , 200 μm , 10
λ	Optical wavelength	650 nm
\vec{L}^T (cm)	Inter-plane distances	[31.5 30.75 0.9]
\vec{L}_a^T (cm)	Plane-to-Lens distances	[21 21]
\vec{f}^T (mm)	Focal lengths of the lenses	[63 63]

In this article, the increasing interference complexity and non-classical nature of MPD based time-domain entanglement resources are characterized by utilizing V_j and by observing the magnitudes of the interfering paths defined as $P_{E,n}(j) \equiv \int dx_j |\Psi_{j,n}(x_j)|^2$ for each n th path. Therefore, more paths with large magnitudes and V_j emphasize increasing interference and non-classicality. Characterizing the correlation between the distribution of path magnitudes and V_j is an open issue since the behavior is highly set-up specific as observed in Section VI. On the other hand, path magnitudes throughout the whole plane may not reflect their localized characteristics such as effecting some sample locations more compared with the others. Therefore, it is an open issue to characterize the interference complexity in terms of the intensity distribution of the paths while the path magnitudes are taken as a reference for simplicity in this article.

VI. NUMERICAL ANALYSIS

MPD set-up with two diffraction planes and single sensor plane is numerically analyzed for both Gaussian and HG sources with beam width and waist sizes of $\sigma_0 = 20 \mu\text{m}$ and $W_0 = 200 \mu\text{m}$, respectively. The detailed set-up parameters are shown in Table I while the set-up is shown in Fig. 4 with $N = 3$ planes. The source waveforms are shown in Figs. 5(a) and (b), respectively. HG order is set to $l = 10$ with highly oscillatory and negative initial V_0 of 1.076. The wavelength of the light is chosen in the red spectrum of $\lambda = 650 \text{ nm}$ while the low cost laser sources are commercially available in a wide spread manner.

Two different set-ups composed of LCT and FSP systems as shown in Figs. 4(a) and (b), respectively, are compared where the LCT system includes thin lenses between the diffraction planes while not included in the FSP system. The kernel based on HO in (8) giving FRFT as a

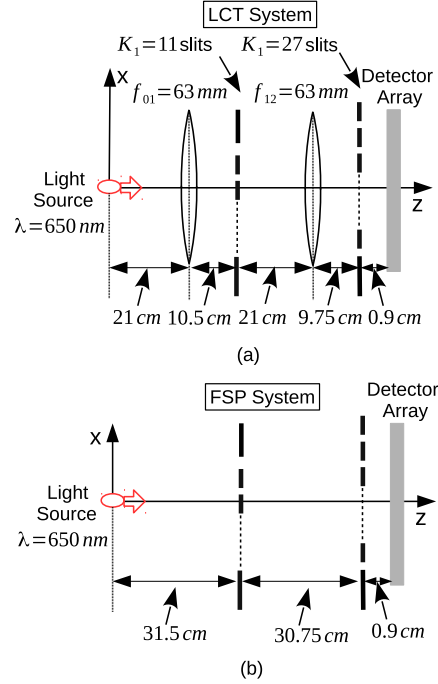


Fig. 4. Photonic QPC set-up with Gaussian and HG classical monochromatic light source with $\lambda = 650$ nm, two planes for diffraction with the number of slits $K_1 = 11$ and $K_2 = 27$, respectively, and specific set-up of (a) LCT and (b) FSP design with the only difference of the existence of thin-lenses of focal length of 63 mm in LCT system.

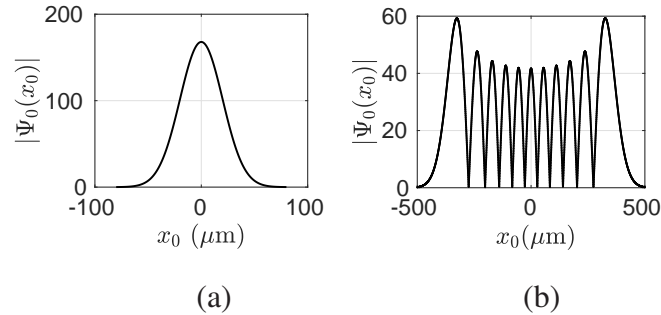


Fig. 5. (a) Gaussian and (b) Hermite-Gaussian (order $l = 10$) source waveforms with $\sigma_0 = 20$ μm and $W_0 = 200$ μm , respectively.

special case of general LCT formulation is not numerically analyzed since LCT based system is a more general version while various combinations including FRFT systems are applicable with the formulation in Tables II and III in Appendix D. Therefore, two different set-ups with the kernels K_{FS} in (9) and $K_{LCT}^{a,b,c,d}$ in (11) for the inter-plane propagation are compared for the same design of slit and plane set-up. The distances of the first plane to the first lens and the second plane to the second lens are denoted with the vector $\vec{L}_a^T \equiv [L_{a,01} \ L_{a,12}]$ where both the

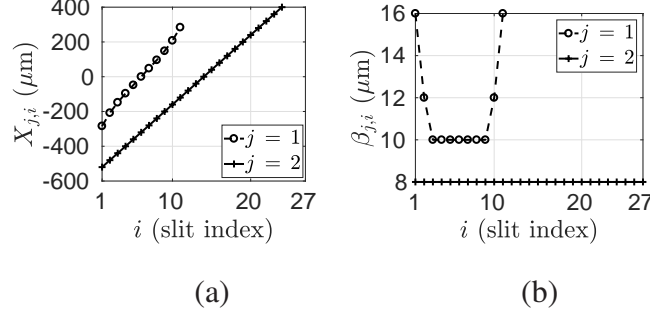


Fig. 6. (a) Slit positions with $K_1 = 11$ and $K_2 = 27$ slits (b) and the widths $\tilde{\beta}_{j,i}$ for $j \in [1, 2]$ and $i \in [1, K_j]$.

distances are set to 21 cm while the lenses of the focal length $\vec{f}^T \equiv [f_{01} \ f_{12}] = [63 \ 63]$ mm focus the light intensity to more compact areas on the consecutive planes compared with FSP. It is assumed that the propagation between the second and third planes includes only FSP without any thin lens to simplify the set-up. $K_1 = 11$ and $K_2 = 27$ slits are used on the first and second planes, respectively. The slit positions and widths on the first plane, as shown in Figs. 6(a) and (b), respectively, are adapted to the maximum intensity locations of HG source propagation on the first plane in LCT system while the ones on the second plane are chosen uniformly with the separation of $40 \mu\text{m}$ and the width of $\tilde{\beta}_{2,j} \equiv \beta_2 = 8 \mu\text{m}$. $K_{LCT}^{a_{01}, b_{01}, c_{01}, d_{01}}$ and $K_{LCT}^{a_{12}, b_{12}, c_{12}, d_{12}}$ are calculated by using (16).

FSP has less control over the propagation of light compared with LCT based Fourier optics. FSP spreads the light intensity without any tuning to the slit positions by reducing the probability of the particle to reach to the consecutive planes after diffraction. Therefore, in numerical analysis, LCT is shown to improve the probability of the particle detection on the sensor plane (P_E) and also the negative volume of Wigner function compared with FSP. The vectors of $P_E(j)$ and V_j composed of the values on the first, second and third (sensor) planes for Gaussian sources are denoted with $\vec{P}_E^{G,FSP}$ and $\vec{V}^{G,FSP}$, respectively, for FSP while with $\vec{P}_E^{G,LCT}$ and $\vec{V}^{G,LCT}$ for LCT. The cases with HG sources are denoted with the superscript of *HG*. It is an open issue to adapt LCT parameters with respect to any given set-up including inter-plane distances, slit locations and widths in a way to maximize the interference and the probability of the particle reaching to the sensor plane.

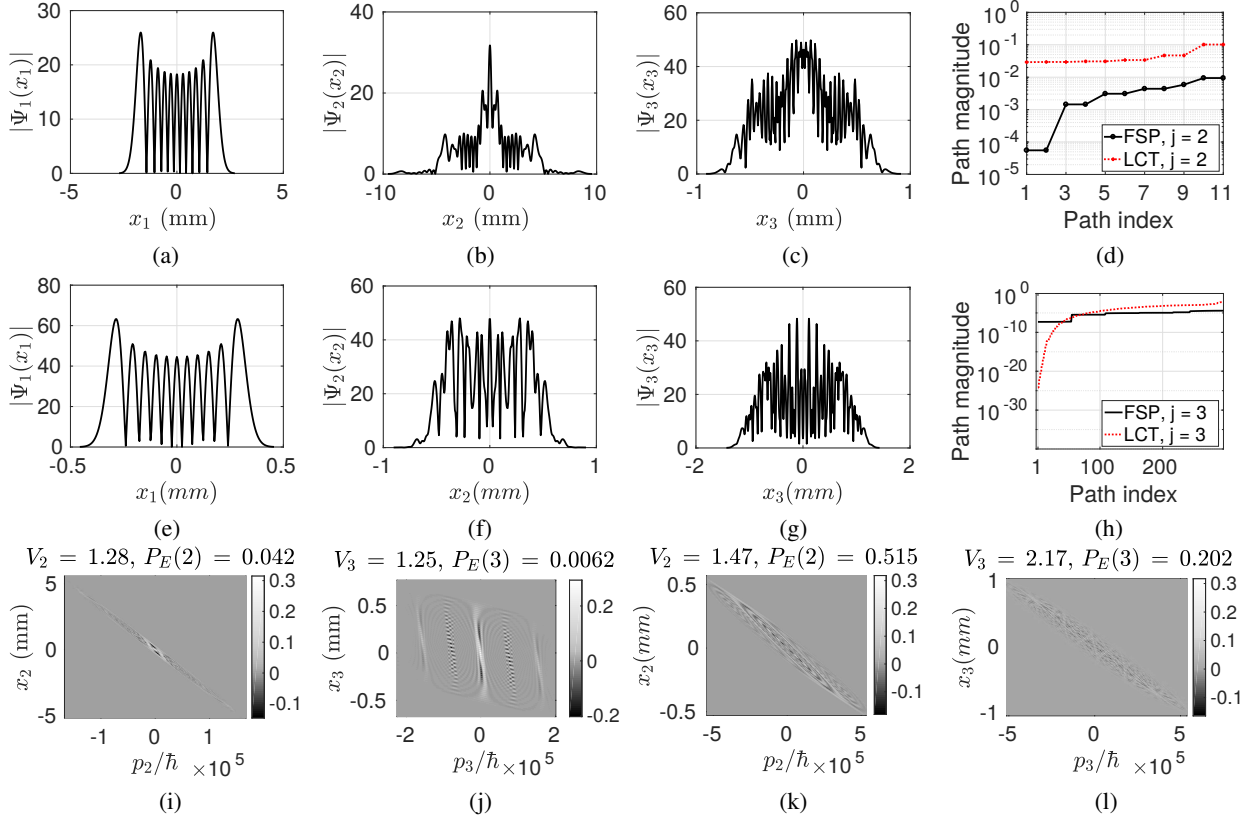


Fig. 7. HG source with the order of $l = 10$ and $W_0 = 200 \mu\text{m}$ is utilized where the resulting spatial domain waveforms on the planes with the indices (a) $j = 1$, (b) $j = 2$ and (c) $j = 3$ for FSP, and (e) $j = 1$, (f) $j = 2$ and (g) $j = 3$ for LCT. $P_E(n, j)$ for (d) $j = 2$ and (h) $j = 3$. Scaled Wigner distribution $\hbar \times W_j(x_j, p_j)$ for FSP on the planes with (i) $j = 2$ and (j) $j = 3$, and for LCT with (k) $j = 2$ and (l) $j = 3$.

A. Hermite-Gaussian Sources

The waveforms on the three planes in spatial domain are shown in Figs. 7(a), (b), (c) and 7(e), (f), (g) for FSP and LCT cases, respectively. It is observed that LCT focuses the light better on the slit locations while FSP reduces P_E significantly. $\vec{P}_E^{HG,LCT} = [1 \ 0.515 \ 0.202]$ is much more improved compared with $\vec{P}_E^{HG,FSP} = [1 \ 0.042 \ 0.0062]$. The magnitudes of the interfering paths are shown in Figs. 7(d) and (h), for $j = 2$ and $j = 3$, respectively, while Wigner distributions on the second and third planes scaled with \hbar are shown in Figs. 7(i) and (j) for FSP and, (k) and (l) for LCT. It is observed that LCT provides significantly larger path magnitudes while $\vec{V}^{HG,LCT} = [1.076 \ 1.47 \ 2.17]$ is also improved compared with $\vec{V}^{HG,FSP} = [1.076 \ 1.28 \ 1.25]$. Observe that HG source has already negative Wigner volume of 1.076 which is much further improved by LCT set-up compared with FSP.

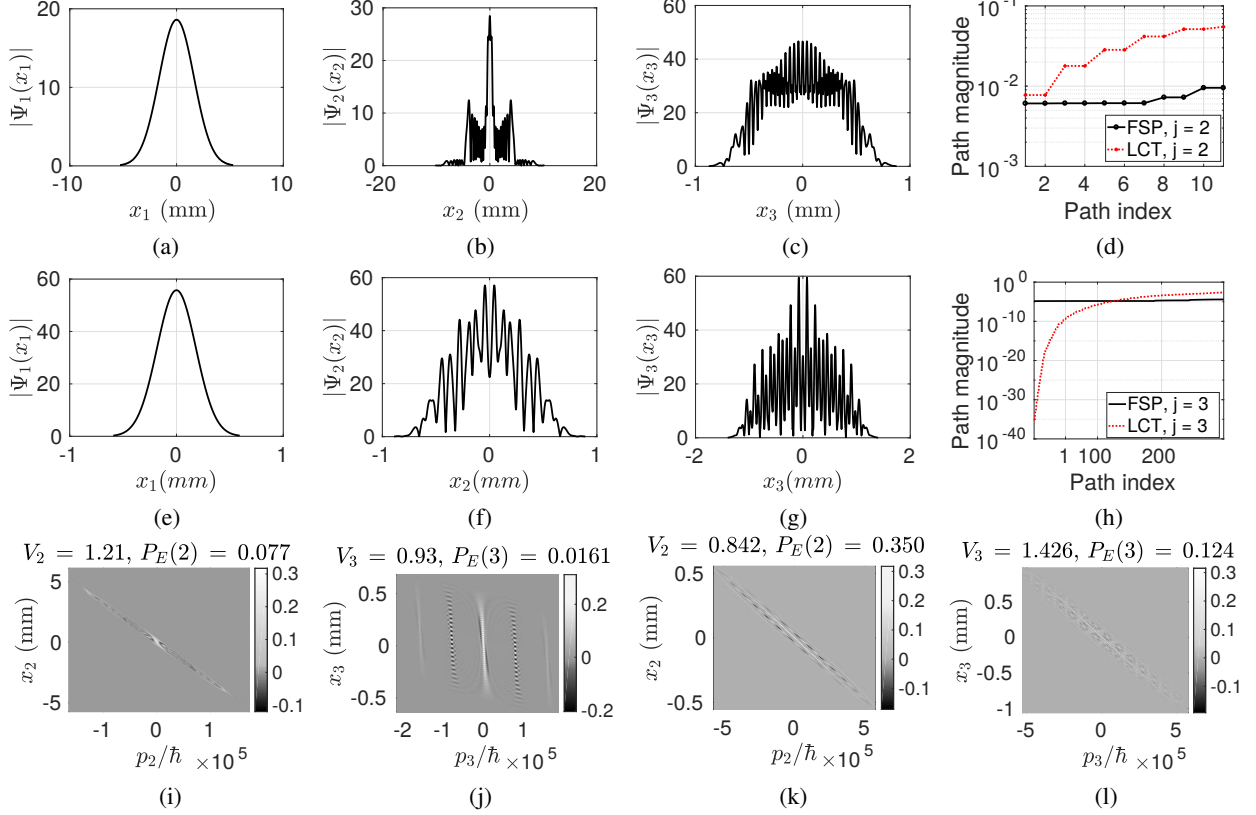


Fig. 8. Gaussian source with $\sigma_0 = 20 \mu\text{m}$ is utilized where the resulting spatial domain waveforms on the planes with the indices (a) $j = 1$, (b) $j = 2$ and (c) $j = 3$ for FSP, and (e) $j = 1$, (f) $j = 2$ and (g) $j = 3$ for LCT. $P_E(n, j)$ for (d) $j = 2$ and (h) $j = 3$. Scaled Wigner distribution $\hbar \times W_j(x_j, p_j)$ for FSP on the planes with (i) $j = 2$ and (j) $j = 3$, and for LCT with (k) $j = 2$ and (l) $j = 3$.

B. Gaussian Sources

The waveforms in spatial domain for Gaussian sources are shown in Figs. 8(a), (b), (c) and 8(e), (f), (g) for FSP and LCT cases, respectively. $\vec{P}_E^{G,LCT} = [1 \ 0.35 \ 0.124]$ and $\vec{P}_E^{G,FSP} = [1 \ 0.077 \ 0.00161]$ values are obtained where the magnitudes of the interfering paths are shown in Figs. 8(d) and (h), for $j = 2$ and $j = 3$, respectively. Similar to the HG sources, LCT improves diffraction probabilities significantly compared with FSP. Wigner distributions scaled with \hbar are shown in Figs. 8(i), (j), (k) and (l) having different characteristics compared with HG case in Figs. 7(i), (j), (k) and (l). It is similarly observed that LCT provides significantly larger path magnitudes. $\vec{V}^{G,LCT} = [0 \ 0.842 \ 1.426]$ and $\vec{V}^{G,FSP} = [0 \ 1.21 \ 0.93]$ are obtained with increasing interference complexity through diffraction on consecutive planes in LCT case while starting with purely classical Gaussian source of zero negative Wigner volume. V_2 of 0.842 for LCT

is smaller than 1.21 for FSP on the second plane. This is due to the both the specific set-up parameters and more diverse distribution of the path magnitudes in LCT after diffraction from the first plane as shown in Fig. 8(d). It becomes more difficult on the third plane to correlate the distribution of the path magnitudes shown in Fig. 8(h) with $V_N = V_3$ shown in Figs. 8(j) and (l). In other words, complexity behaves differently compared with the transmission probability while requiring simultaneous maximization depending on specific set-up as an open issue as discussed in Section V.

VII. OPEN ISSUES AND DISCUSSION

There are some open issues to best exploit photonic MPD for QC and QComm purposes. Mathematical formulation correlating the specific set-up parameters to the path magnitude distribution and the negative volume of Wigner function is an open issue. Iterative formulation of the vectors $\vec{h}_{N-1,n}$, $\vec{\gamma}_{N-1,n}$, $\vec{\eta}_{N-1,n}$ and the matrices $\tilde{\mathbf{H}}_{N-1,n}^{HO/G}$, $\tilde{\mathbf{H}}_{N-1,n}^{LCT/G}$ and $\tilde{\mathbf{H}}_{N-1,n}^{LCT/HG}$ in (18), (22) and (24) are complicated as shown in Appendices with complicated parameters and iterations in Tables II and III in Appendix D. Therefore, adapting the physical set-up parameters to the desired form of partial sum of Riemann theta function for the target number theoretical problem, and characterizing the path distributions and the negative volume of Wigner function explicitly are important open issues.

Realizing perfectly Gaussian slits compared with the conventional rectangular apertures is an important open issue for matching the experimental results with the proposed theoretical model. However, any slit structure can be represented as a composition of Gaussian slits by using the method defined in [27] and applied successfully in optical diffraction theory and experiments [28], [29]. The one dimensional slit function $G(x)$ is represented as follows:

$$G(x) \approx \sum_{i=1}^K a_i \exp(-x^2 / 2 \beta_i^2) \quad (28)$$

where a_i and β_i are found with optimization based on the experimental measurement results while increasing K provides more accurate results. If the perfect Gaussian slits are replaced with the superposition in (28), then the summations in (18), (22) and (24) should be made for each β_i of the single slit increasing the computational complexity of the QPC output exponentially. The functional form with partial sum of Riemann theta function should be calculated and summed for each combination of β_i through all the slits. Therefore, non-Gaussian slits realize the solutions of

much harder computational complexity problems while it is an open issue to utilize for practical purposes.

There are some factors reducing the compatibility between the theory and practice. These include imperfection in optical set-up, e.g., finite size lens effects, planar thickness, characterization of slit functions, sources and detector efficiency. The theoretical model should be extended including all the set-up parameters having diverging effects on the final intensity distribution. Similarly, the effects of exotic paths, i.e., trajectories between the slits on the same plane, should be included in the mathematical model as thoroughly discussed in [1], [14], [30].

Another open issue is related to utilize measurements on all the sensor planes for computational purposes not only the final sensor plane since they include diffraction through previous planes. Theoretical models are required to exploit the sensor measurement results. Besides that, mirror based planar diffraction structures could prevent the absorption in previous planes while resulting longer length MPD set-up for the reflecting waves through the planes back and forth. Theoretical model and system design are necessary for mirror based MPD architectures.

VIII. CONCLUSIONS

In this article, MPD architecture for arbitrary Fourier optical set-ups is defined, theoretically modeled and numerically analyzed for implementing a scalable and simple photonic platform for QC and QComm applications. LCTs between diffraction planes are implemented with quantum Fourier optics while utilizing coherent Gaussian and HG source beams as the widely available standard laser sources. Numerical analysis is provided showing the performance improvement and flexibility of LCT based system design compared with FSP. Photonic MPD based on Fourier optics is the simplest linear optical system combining the advantages of low complexity, classical source and detection mechanisms and the maturity of Fourier optics since the last century with the globally available resources for the development of the proposed design.

APPENDIX A

MATRIX FORMULATION FOR HO/LCT SYSTEM WITH GAUSSIAN SOURCES

The following formulation is valid for both HO and LCT based design with Gaussian sources with the corresponding parameters defined in Table II in Appendix D. The elements in the vector

$\vec{h}_{N-1,n} = \vec{c}_{N-1,n} + \iota \vec{d}_{N-1,n}$ are defined as follows:

$$\begin{bmatrix} \vec{c}_{N-1,n}^T \\ \vec{d}_{N-1,n}^T \end{bmatrix} = \begin{bmatrix} \vec{v}_{0,N-1,n} & \vec{v}_{1,N-1,n} & \dots & \vec{v}_{N-2,N-1,n} \end{bmatrix} \quad (29)$$

where $\vec{v}_{k,j,n}$ for $k \in [0, j-1]$ is given as follows:

$$\vec{v}_{k,j,n} \equiv \left(\prod_{i=1}^{j-1-k} \begin{bmatrix} \tilde{p}_{4,j+1-i,n} & \tilde{p}_{5,j+1-i,n} \\ -\tilde{p}_{5,j+1-i,n} & \tilde{p}_{4,j+1-i,n} \end{bmatrix} \right) \begin{bmatrix} \tilde{\zeta}_{k+1,c,n} \\ \tilde{\zeta}_{k+1,d,n} \end{bmatrix} \quad (30)$$

where the matrix multiplication $\prod_{i=1}^k \mathbf{U}_i$ denotes $\mathbf{U}_1 \mathbf{U}_2 \dots \mathbf{U}_k$ for any matrix \mathbf{U}_i for $i \in [1, k]$ and $\tilde{p}_{4,j,n}$, $\tilde{p}_{5,j,n}$, $\tilde{\zeta}_{j,c,n}$ and $\tilde{\zeta}_{j,d,n}$ for $j \in [1, N-1]$ are defined in Table II in Appendix D. Assume that $\text{diag}\{\vec{y}_1, \dots, \vec{y}_K\}$ and $\text{diag}\{\mathbf{y}_1, \dots, \mathbf{y}_K\}$ define the operators creating block diagonal matrices by putting the vectors \vec{y}_j and the matrices \mathbf{y}_j for $j \in [1, K]$, respectively, (all the vectors or the matrices having the same dimensions) to the main diagonal and making zero the remaining elements. The matrix $\tilde{\mathbf{H}}_{N-1,n}^{HO/G}$ is more simplified as follows compared with the more complicated form achieved for electron based FSP in [1]:

$$\tilde{\mathbf{H}}_{N-1,n}^{HO/G,R} = \tilde{\mathbf{D}}_{a,N-1,n}^{HO/G,R} + \begin{bmatrix} \tilde{\mathbf{V}}_{N-1,n}^T \tilde{\mathbf{D}}_{b,N-1,n}^{HO/G,R} \tilde{\mathbf{V}}_{N-1,n} & \vec{0}_{N-2} \\ \vec{0}_{N-2}^T & 0 \end{bmatrix} + \begin{bmatrix} \vec{0}_{N-2}^T & 0 \\ \tilde{\mathbf{D}}_{c,N-1,n}^{HO/G,R} \tilde{\mathbf{V}}_{N-1,n} & \vec{0}_{N-2} \end{bmatrix} \quad (31)$$

where the diagonal matrices are defined as follows:

$$\tilde{\mathbf{D}}_{a,N-1,n}^{HO/G,R} = \text{diag}\{\tilde{p}_{1,1,n}, \tilde{p}_{1,2,n}, \dots, \tilde{p}_{1,N-1,n}\} \quad (32)$$

$$\tilde{\mathbf{D}}_{b,N-1,n}^{HO/G,R} = \text{diag}\{\tilde{\mathbf{K}}_{2,b,n}, \tilde{\mathbf{K}}_{3,b,n}, \dots, \tilde{\mathbf{K}}_{N-1,b,n}\} \quad (33)$$

$$\tilde{\mathbf{D}}_{c,N-1,n}^{HO/G,R} = \text{diag}\{\tilde{k}_{2,c,n}^T, \tilde{k}_{3,c,n}^T, \dots, \tilde{k}_{N-1,c,n}^T\} \quad (34)$$

where 2×2 block $\tilde{\mathbf{K}}_{j,b,n}$ and 1×2 vector $\tilde{k}_{j,c,n}^T$ are defined as follows for $j \in [2, N-1]$:

$$\tilde{\mathbf{K}}_{j,b,n} = \frac{\tilde{\beta}_{j,n}^2 \tilde{p}_{3,j,n}}{2} \begin{bmatrix} 1 & \iota \\ \iota & -1 \end{bmatrix} \quad (35)$$

$$\tilde{k}_{j,c,n}^T = \tilde{p}_{3,j,n} \begin{bmatrix} 1 & \iota \end{bmatrix} \quad (36)$$

$\tilde{\mathbf{V}}_{N-1,n}$ is a lower triangular block matrix defined as follows:

$$\begin{bmatrix} \tilde{v}_{0,1,n} & \vec{0}_2 & \vec{0}_2 & \dots & \vec{0}_2 \\ \tilde{v}_{0,2,n} & \tilde{v}_{1,2,n} & \vec{0}_2 & \dots & \vec{0}_2 \\ \tilde{v}_{0,3,n} & \tilde{v}_{1,3,n} & \tilde{v}_{2,3,n} & \dots & \vec{0}_2 \\ \vdots & \vdots & \vdots & \ddots & \vec{0}_2 \\ \tilde{v}_{0,N-2,n} & \tilde{v}_{1,N-2,n} & \tilde{v}_{2,N-2,n} & \dots & \tilde{v}_{N-3,N-2} \end{bmatrix} \quad (37)$$

Expanding $\tilde{\mathbf{H}}_{N-1,n}^{HO/G}$ in terms of real and imaginary parts is achieved by finding the real and imaginary parts of $\tilde{p}_{1,j,n}$ for $j \in [1, N-1]$ and $\tilde{p}_{3,j,n}$ for $j \in [2, N-1]$, and $\tilde{\mathbf{K}}_{j,b,n}$ and $\tilde{k}_{j,c,n}$ for $j \in [2, N-1]$ since $\tilde{\mathbf{V}}_{N-1,n}$ is a real matrix. This is easily achieved by using the explicit forms of $\tilde{p}_{1,j,n}$ and $\tilde{p}_{3,j,n}$ in Table II in Appendix D.

APPENDIX B

INTEGRAL EQUALITY OF HERMITE POLYNOMIAL

The formulation in (19) is obtained by using the integral equality for Hermite polynomials (Section 16.5 in [25]) in an iterative manner along the planes:

$$\int dx \exp\left(\frac{-(x-y)^2}{2}\right) H_l\left(\frac{ax}{\sqrt{2}}\right) = \sqrt{2\pi} (1-a^2)^{l/2} H_l\left(\frac{ay}{\sqrt{2(1-a^2)}}\right) \quad (38)$$

APPENDIX C

MATRIX FORMULATION FOR LCT SYSTEM WITH HERMITE-GAUSSIAN SOURCES

The parameters $\tilde{\gamma}_{j,j+1,n}$ in $\tilde{\gamma}_{N-1,n}^{\mathcal{Z}} \equiv [\tilde{\gamma}_{12,n} \tilde{\gamma}_{23,n} \dots \tilde{\gamma}_{N-1,N,n}]$ and $\tilde{\eta}_{N-1,n}^{\mathcal{Z}}$ utilized in (20) are defined as follows:

$$\tilde{\eta}_{N-1,n}^{\mathcal{Z}} \equiv \begin{bmatrix} \tilde{\Xi}_{N-2,n}^{\mathcal{Z}} & 0 \end{bmatrix} \begin{bmatrix} \tilde{\Lambda}_{N-2,n} & \vec{0}_{N-2} \\ \vec{0}_{N-2}^T & 0 \end{bmatrix} + \tilde{\epsilon}_{N-1,n}^{\mathcal{Z}} \quad (39)$$

where the following are defined:

$$\tilde{\Lambda}_{N-2,n} \equiv [\vec{G}_1 \ \vec{G}_2 \ \dots \ \vec{G}_{N-2}]^T \quad (40)$$

$$\vec{G}_k \equiv [(\vec{\gamma}_{k,n}^*)^T \ \vec{0}_{N-2-k}^T]^T \quad (41)$$

$$\vec{\gamma}_{k,n}^* \equiv [{}^k\tilde{\gamma}_{1,2,n}^* \ {}^k\tilde{\gamma}_{2,3,n}^* \ \dots \ {}^k\tilde{\gamma}_{k,k+1,n}^*]^T \quad (42)$$

$$\vec{\varepsilon}_{N-1,n} \equiv [\tilde{\varepsilon}_{12,n} \ \tilde{\varepsilon}_{23,n} \ \dots \ \tilde{\varepsilon}_{N-1,N,n}]^T \quad (43)$$

$$\vec{\Xi}_{N-2,n} \equiv [\tilde{\Xi}_{12,n} \ \tilde{\Xi}_{23,n} \ \dots \ \tilde{\Xi}_{N-2,N-1,n}]^T \quad (44)$$

$$\tilde{\Xi}_{j,j+1,n} \equiv \tilde{h}_{c,j+1,j+2,n} \prod_{k=j+2}^{N-1} \tilde{h}_{a,k,k+1,n} \quad (45)$$

where $\vec{\Xi}_{N-2,n}^T$ for $N > 2$, $\tilde{\Xi}_{j,j+1,n}$ for $j \geq 1$, and $\tilde{\gamma}_{j,j+1,n} = {}^{N-1}\tilde{\gamma}_{j,j+1,n}^*$ while ${}^l\tilde{\gamma}_{j,j+1,n}^*$ and $\tilde{\varepsilon}_{j,j+1,n}$ are defined as follows:

$${}^l\tilde{\gamma}_{j,j+1,n}^* \equiv \begin{cases} \tilde{v}_{a,j,j+1,n} \prod_{k=j+1}^l \tilde{\beta}_{k,n}^2 \tilde{v}_{a,k,k+1,n}, & j \geq 2 \\ \tilde{v}_{a,12,n} \prod_{k=2}^l \tilde{\beta}_{k,n}^2 \tilde{v}_{a,k,k+1,n}, & j = 1 \end{cases} \quad (46)$$

$$\tilde{\varepsilon}_{j,j+1,n} \equiv \begin{cases} \tilde{h}_{b,j,j+1,n} \prod_{k=j+1}^{N-1} \tilde{h}_{a,k,k+1,n}, & j \geq 2 \\ \tilde{h}_{a,12,n} \prod_{k=2}^{N-1} \tilde{h}_{a,k,k+1,n}, & j = 1 \end{cases} \quad (47)$$

where $\tilde{\gamma}_{12,n} \equiv \tilde{v}_{a,12,n}$ and $\tilde{\varepsilon}_{12,n} \equiv \tilde{h}_{a,12,n}$ for $N = 2$, and ${}^1\tilde{\gamma}_{1,2,n}^* \equiv \tilde{v}_{a,12,n}$. $\tilde{\mathbf{H}}_{N-1,n}^{LCT/HG}$ equals to the following:

$$-\tilde{\theta}_{12,n} \begin{bmatrix} 1 & \vec{0}_{N-2}^T \\ \vec{0}_{N-2} & \mathbf{0}_{N-2} \end{bmatrix} + \sum_{j=2}^{N-1} \begin{bmatrix} \tilde{\mathbf{H}}_{j,n}^{LCT/HG,\chi} & \mathbf{0}_{j,N-1-j} \\ \mathbf{0}_{N-1-j,j} & \mathbf{0}_{N-1-j} \end{bmatrix} \quad (48)$$

where $\tilde{\mathbf{H}}_{k,n}^{LCT/HG,\chi}$ is the following:

$$\begin{aligned} \tilde{\mathbf{H}}_{k,n}^{LCT/HG,\chi} &= \tilde{\theta}_{a,k,k+1,n} \begin{bmatrix} \vec{\gamma}_{k-1,n}^* (\vec{\gamma}_{k-1,n}^*)^T & \vec{0}_{k-1} \\ \vec{0}_{k-1}^T & 0 \end{bmatrix} \\ &+ \tilde{\theta}_{b,k,k+1,n} \begin{bmatrix} \mathbf{0}_{k-1} & \vec{\gamma}_{k-1,n}^* \\ \vec{0}_{k-1}^T & 0 \end{bmatrix} + \tilde{\theta}_{c,k,k+1,n} \begin{bmatrix} \mathbf{0}_{k-1} & \vec{0}_{k-1} \\ \vec{0}_{k-1}^T & 1 \end{bmatrix} \end{aligned} \quad (49)$$

APPENDIX D

ITERATION PARAMETERS FOR FPI MODELING

Some variables and constants used in Tables II and III (not defined in the tables) are the following: $\iota \equiv \sqrt{-1}$, $x_{j,n}$ denotes $X_{j,s_{n,j}}$, $\lambda_0 = \hbar t_{0,1}$, $\tilde{\tau}_{a,j,n} \equiv b_{j,j+1} \tilde{u}_{j-1,j,n} + \iota \pi a_{j,j+1}$ for $j \in [2, N-1]$, $\tau_{a,1} \equiv b_{12} \tilde{u}_{01} + \iota \pi a_{12}$, $\tilde{\Gamma}_{1,n} = 2 \tilde{\beta}_{1,n}^2 b_{1,2} \tilde{g}_{0,1}^2 + \tilde{\tau}_{1,n}$, $\alpha_j = \omega t_{j,j+1}$ for $j \in [0, N-1]$, $\hat{m}_j = m_\lambda / \sin(\omega t_{j,j+1})$ and $\tilde{\lambda}_{j,n}^*$ as the conjugate of $\tilde{\lambda}_{j,n}$ for real values of $(a_{j,j+1}, b_{j,j+1}, c_{j,j+1}, d_{j,j+1})$.

REFERENCES

- [1] B. Gulbahar, “Quantum path computing: computing architecture with propagation paths in multiple plane diffraction of classical sources of fermion and boson particles,” *Quantum Information Processing*, vol. 18, no. 6, p. 167, 2019.
- [2] B. Gulbahar, “Quantum entanglement and interference in time with multi-plane diffraction and violation of Leggett-Garg inequality without signaling,” *arXiv preprint arXiv:1808.06477*, 2018.
- [3] B. Gulbahar and G. Memisoglu, “Quantum spatial modulation of optical channels: Quantum boosting in spectral efficiency,” *IEEE Communications Letters*, vol. 1, pp. 1–1, 2019. doi: 10.1109/LCOMM.2019.2932671
- [4] J. Carolan et al., “Universal linear optics,” *Science*, vol. 349, no. 6249, pp. 711–716, 2015.
- [5] X. Wang et al., “Experimental ten-photon entanglement,” *Phys. Rev. Lett.*, vol. 117, no. 21, pp. 210502-1–210502-6, 2016.
- [6] J. Wang et al., “Multidimensional quantum entanglement with large-scale integrated optics,” *Science*, vol. 360, no. 6386, pp. 285–291, 2018.
- [7] H. Wang et al., “Toward scalable boson sampling with photon loss,” *Phys. Rev. Lett.*, vol. 120, no. 23, pp. 230502-1–230502-6, 2018.
- [8] K. Sawada and S. Walborn, “Experimental quantum information processing with the Talbot effect,” *Journal of Optics*, vol. 20, no. 7, p. 075201, 2018.
- [9] M. R. Barros, A. Ketterer, O. J. Farías and S. P. Walborn, “Free-space entangled quantum carpets,” *Phys. Rev. A*, vol. 95, no. 4, p. 042311, 2017.
- [10] D. S. Tasca, Ł. Rudnicki, R. S. Aspdén, M. J. Padgett, P. S. Ribeiro and S. P. Walborn, “Testing for entanglement with periodic coarse graining,” *Phys. Rev. A*, vol. 97, no. 4, p. 042312, 2018.
- [11] H. Ozaktas, Z. Zalevsky and M. A. Kutay, *The Fractional Fourier Transform with Applications in Optics and Signal Processing*, Chichester, UK: John Wiley and Sons, Jan. 2001.
- [12] J. J. Healy, M. A. Kutay, H. M. Ozaktas and J. T. Sheridan, *Linear Canonical Transforms: Theory and Applications*, Springer, vol. 198, 2015.
- [13] E. A. Santos, F. Castro and R. Torres, “Huygens-Fresnel principle: Analyzing consistency at the photon level,” *Phys. Rev. A*, vol. 97, no. 4, p. 043853, 2018.
- [14] R. Sawant, J. Samuel, A. Sinha, S. Sinha and U. Sinha, “Nonclassical paths in quantum interference experiments,” *Phys. Rev. Lett.*, vol. 113, p. 120406, Sep. 2014.
- [15] F. Pampaloni and J. Enderlein, “Gaussian, Hermite-Gaussian, and Laguerre-Gaussian beams: A primer,” *arXiv preprint arXiv: 0410021v1*, 2004.
- [16] A. Kenfack and K. Życzkowski, “Negativity of the Wigner function as an indicator of non-classicality,” *Journal of Optics B: Quantum and Semiclassical Optics*, vol. 6, no. 10, p. 396, 2004.

TABLE II

ITERATION PARAMETERS FOR FPI MODELING OF MPD WITH THE KERNELS K_{HO} AND $K_{LCT}^{(a,b,c,d)}$ FOR GAUSSIAN SOURCES

	Formula for K_{HO} based MPD ($\omega t_{j,j+1} / \pi \notin \mathbb{Z}$)	Formula for $K_{LCT}^{(a,b,c,d)}$ based MPD ($b_{j,j+1} \neq 0$)
$\Psi_0(x_0) = \exp(-x_0^2 / (2\sigma_0^2)) / \sqrt{\sigma_0 \sqrt{\pi}}$ & $\Psi_1(x_1) = \chi_0 \exp(A_0 x_1^2 + \iota B_0 x_1^2)$		
A_0	$-\widehat{m}_0^2 \sigma_0^2 / (2 \cos^2(\alpha_0) \widehat{m}_0^2 \sigma_0^4 + 2 \lambda_0^2)$	$-2 \pi^2 \sigma_0^2 / (4 \pi^2 a_{01}^2 \sigma_0^4 + b_{01}^2)$
B_0	$\cos(\alpha_0) \widehat{m}_0 (\lambda_0^2 - \sin^2(\alpha_0) \widehat{m}_0^2 \sigma_0^4) / (2 \lambda_0 (\cos^2(\alpha_0) \widehat{m}_0^2 \sigma_0^4 + \lambda_0^2))$	$\pi d_{01} / b_{01} - 4 \pi^3 a_{01} \sigma_0^4 / (b_{01} (4 \pi^2 a_{01}^2 \sigma_0^4 + b_{01}^2))$
χ_0	$\pi^{-1/4} \sqrt{\widehat{m}_0 \sigma_0} / (\cos(\alpha_0) \widehat{m}_0 \sigma_0^2 + \iota \lambda_0)$	$\exp(-\iota \pi / 4) \sqrt{2 \sqrt{\pi} \sigma_0} / (b_{01} - 2 \iota \pi a_{01} \sigma_0^2)$
$\Psi_{2,n}(x_2) = \chi_0 \chi_{1,n} \exp(\widetilde{A}_{1,n} x_2^2 + \iota \widetilde{B}_{1,n} x_2^2 + C_{1,n} x_2 + \iota D_{1,n} x_2)$		
$\widetilde{A}_{1,n}$	$\widetilde{\beta}_{1,n}^2 \widehat{m}_{12}^2 (2 A_0 \widetilde{\beta}_{1,n}^2 - 1) / (2 \widetilde{\zeta}_{1,n})$	$2 \pi^2 \widetilde{\beta}_{1,n}^2 (2 A_0 \widetilde{\beta}_{1,n}^2 - 1) / \widetilde{\zeta}_{1,n}$
$\widetilde{B}_{1,n}$	$(2 B_0 \widetilde{\beta}_{1,n}^4 \widehat{m}_{12}^2 \cos(2 \alpha_1) + \cos(\alpha_1) \lambda_1 \widehat{m}_{12} \varrho_1) / (2 \widetilde{\zeta}_{1,n})$ $-\widetilde{\beta}_{1,n}^4 \widehat{m}_{12}^3 \cos(\alpha_1) \sin^2(\alpha_1) / (2 \lambda_1 \widetilde{\zeta}_{1,n})$	$\pi (d_{12} \widetilde{\zeta}_{1,n} - 4 \pi \widetilde{\beta}_{1,n}^4 (\pi a_{12} + B_0 b_{12})) / (b_{12} \widetilde{\zeta}_{1,n})$
$\chi_{1,n}, C_{1,n}, D_{1,n}$	$\sqrt{\widetilde{\xi}_{1,n} \exp(\widetilde{\rho}_{1,1,n} x_{1,n}^2)}, \quad \widetilde{\zeta}_{1,c,n} x_{1,n}, \quad \widetilde{\zeta}_{1,d,n} x_{1,n}$	
$\Psi_{j+1,n}(x_{j+1}) = \chi_0 (\prod_{k=1}^j \chi_{k,n}) e^{(A_{j,n} + \iota B_{j,n}) x_{j+1}^2 + (C_{j,n} + \iota D_{j,n}) x_{j+1}}$ for $j \in [2, N-1]$		
$\widetilde{\rho}_{2,j,n}, \widetilde{\rho}_{3,j,n},$ $\widetilde{\rho}_{4,j,n}, \widetilde{\rho}_{5,j,n}$	$-\widetilde{\beta}_{j,n}^2 \lambda_j / (2 \iota \widetilde{\zeta}_{j,n}), -\lambda_j / (\iota \widetilde{\zeta}_{j,n}),$ $\widetilde{\beta}_{j,n}^2 \widetilde{\zeta}_{j,c,n}, -\widetilde{\beta}_{j,n}^2 \widetilde{\zeta}_{j,d,n}$	$\widetilde{\beta}_{j,n}^2 \widetilde{\zeta}_{j,n} / (2 \widetilde{\zeta}_{j,n}), \widetilde{\zeta}_{j,n} / \widetilde{\zeta}_{j,n},$ $\widetilde{\beta}_{j,n}^2 \widetilde{\zeta}_{j,c,n}, -\widetilde{\beta}_{j,n}^2 \widetilde{\zeta}_{j,d,n}$
$\widetilde{A}_{j,n}$	$\widetilde{\beta}_{j,n}^2 \widehat{m}_j^2 (2 \widetilde{A}_{j-1,n} \widetilde{\beta}_{j,n}^2 - 1) / (2 \widetilde{\zeta}_{j,n})$	$2 \pi^2 \widetilde{\beta}_{j,n}^2 (2 \widetilde{A}_{j-1,n} \widetilde{\beta}_{j,n}^2 - 1) / \widetilde{\zeta}_{j,n}$
$\widetilde{B}_{j,n}$	$\widehat{m}_j (2 \widetilde{B}_{j-1,n} \widetilde{\beta}_{j,n}^4 \cos(2 \alpha_j) \widehat{m}_j + \cos(\alpha_j) \lambda_j \widetilde{\varrho}_{j,n}) / (2 \widetilde{\zeta}_{j,n})$ $-(\widetilde{\beta}_{j,n}^4 \widehat{m}_j^3 \cos(\alpha_j) \sin^2(\alpha_j)) / (2 \lambda_j \widetilde{\zeta}_{j,n})$	$\frac{\pi (d_{j,j+1} \widetilde{\zeta}_{j,n} - 4 \pi \widetilde{\beta}_{j,n}^4 (\pi a_{j,j+1} + \widetilde{B}_{j-1,n} b_{j,j+1}))}{(b_{j,j+1} \widetilde{\zeta}_{j,n})}$
$C_{j,n}, D_{j,n}$	$\widetilde{\zeta}_{j,c,n} x_{j,n} + \widetilde{\rho}_{4,j,n} C_{j-1,n} + \widetilde{\rho}_{5,j,n} D_{j-1,n}, \quad \widetilde{\zeta}_{j,d,n} x_{j,n} - \widetilde{\rho}_{5,j,n} C_{j-1,n} + \widetilde{\rho}_{4,j,n} D_{j-1,n}$	
$\chi_{j,n}$	$\sqrt{\widetilde{\xi}_{j,n} \exp(\widetilde{\rho}_{1,j,n} x_{j,n}^2)} \times \exp(\widetilde{\rho}_{2,j,n} (C_{j-1,n} + \iota D_{j-1,n})^2) \times \exp(\widetilde{\rho}_{3,j,n} (C_{j-1,n} + \iota D_{j-1,n}) x_{j,n})$	
The following variables defined for $j \in [1, N-1]$		
λ_j or $\widetilde{\lambda}_{j,n}$	$\hbar t_{j,j+1}$	$b_{j,j+1} (\widetilde{A}_{j-1,n} + \iota \widetilde{B}_{j-1,n}) + \iota \pi a_{j,j+1}$
$\widetilde{\rho}_{1,j,n}$	$-(2 \lambda_j (\widetilde{A}_{j-1,n} + \iota \widetilde{B}_{j-1,n}) + \iota \cos(\alpha_j) \widehat{m}_j) / (2 \iota \widetilde{\zeta}_{j,n})$	$\widetilde{\lambda}_{j,n} (b_{j,j+1} - 2 \widetilde{\beta}_{j,n}^2 \widetilde{\lambda}_{j,n}^*) / \widetilde{\zeta}_{j,n}$
$\widetilde{\zeta}_{j,n}, \widetilde{\xi}_{j,n}$	$\widetilde{\beta}_{j,n}^2 (\cos(\alpha_j) \widehat{m}_j + 2 \lambda_j (\widetilde{B}_{j-1,n} - \iota \widetilde{A}_{j-1,n})) + \iota \lambda_j,$ $\widetilde{\beta}_{j,n}^2 \widehat{m}_j / \widetilde{\zeta}_{j,n}$	$b_{j,j+1} (b_{j,j+1} - 2 \widetilde{\beta}_{j,n}^2 \widetilde{\lambda}_{j,n}^*),$ $2 \pi \widetilde{\beta}_{j,n}^2 / (\iota (b_{j,j+1} - 2 \widetilde{\beta}_{j,n}^2 \widetilde{\lambda}_{j,n}^*))$
$\widetilde{\varrho}_{j,n}$	$4 \widetilde{\beta}_{j,n}^4 (\widetilde{A}_{j-1,n}^2 + \widetilde{B}_{j-1,n}^2) - 4 \widetilde{A}_{j-1,n} \widetilde{\beta}_{j,n}^2 + 1$	
$\widetilde{\zeta}_{j,n}$	$4 \widetilde{B}_{j-1,n} \widetilde{\beta}_{j,n}^4 \cos(\alpha_j) \lambda_j \widehat{m}_j + \widetilde{\beta}_{j,n}^4 \cos^2(\alpha_j) \widehat{m}_j^2 + \lambda_j^2 \widetilde{\varrho}_{j,n}$	$b_{j,j+1}^2 \widetilde{\varrho}_{j,n}$ $+ 4 \pi a_{j,j+1} \widetilde{\beta}_{j,n}^4 (\pi a_{j,j+1} + 2 \widetilde{B}_{j-1,n} b_{j,j+1})$
$\widetilde{\zeta}_{j,c,n}$	$\widetilde{\beta}_{j,n}^2 \widehat{m}_j (2 \widetilde{B}_{j-1,n} \lambda_j + \cos(\alpha_j) \widehat{m}_j) / \widetilde{\zeta}_{j,n}$	$4 \pi \widetilde{\beta}_{j,n}^2 (\pi a_{j,j+1} + \widetilde{B}_{j-1,n} b_{j,j+1}) / \widetilde{\zeta}_{j,n}$
$\widetilde{\zeta}_{j,d,n}$	$\lambda_j \widehat{m}_j (2 \widetilde{A}_{j-1,n} \widetilde{\beta}_{j,n}^2 - 1) / \widetilde{\zeta}_{j,n}$	$2 \pi b_{j,j+1} (2 \widetilde{A}_{j-1,n} \widetilde{\beta}_{j,n}^2 - 1) / \widetilde{\zeta}_{j,n}$

[17] G. F. B. Riemann, "Theorie der Abel'schen functionen," *Journal für reine und angewandte Mathematik*, vol. 54, p. 101, 1857.

[18] B. Deconinck, M. Heil, A. Bobenko, M. Van Hoeij and M. Schmies, "Computing Riemann theta functions," *Mathematics of Computation*, vol. 73, no. 247, pp. 1417–1442, 2004.

[19] D. Mumford, "Tata lectures on Theta I," USA: Birkhäuser Boston, 1994.

[20] A. R. Osborne, "Nonlinear Ocean Waves and the Inverse Scattering Transform," UK: Elsevier Academic Press, 2010.

[21] M. A. Nielsen and I. L. Chuang, *Quantum Computation and Quantum Information*, Cambridge University Press, Dec. 2010.

TABLE III

ITERATION PARAMETERS FOR FPI MODELING OF MPD WITH THE KERNEL $K_{LCT}^{(a,b,c,d)}$ FOR HERMITE-GAUSSIAN SOURCES
($b_{j,j+1} \neq 0$)

$\Psi_0(x_0) = (2^{1/4} / \sqrt{W_0 2^l l!}) \exp(-\pi x_0^2 / W_0^2) H_l(\sqrt{2\pi} x_0 / W_0)$ and $\Psi_1(x_1) = \chi_{01} \exp(u_{01} x_1^2) H_l(g_{01} x_1)$									
Symbol	Formula	Symbol	Formula	Symbol	Formula	Symbol	Formula		
g_{01}	$\sqrt{\frac{2\pi W_0^2}{a_{01}^2 W_0^4 + b_{01}^2}}$	u_{01}	$-\frac{\pi W_0^2}{a_{01}^2 W_0^4 + b_{01}^2} + l \left(\frac{\pi d_{01}}{b_{01}} - \frac{(\pi W_0^2)(a_{01} W_0^2)}{b_{01}(a_{01}^2 W_0^4 + b_{01}^2)} \right)$	χ_{01}	$\frac{2^{1/4} \sqrt{W_0}}{\sqrt{2^l l!}} \sqrt{\frac{a_{01} W_0^2 - i b_{01}}{a_{01}^2 W_0^4 + b_{01}^2}} \left(\frac{a_{01} W_0^2 - i b_{01}}{\sqrt{a_{01}^2 W_0^4 + b_{01}^2}} \right)^l$				
$\Psi_{2,n}(x_2) = \chi_{01} \chi_{12,n} \exp(\tilde{u}_{12,n} x_2^2 + v_{12,n} x_2) H_l(\tilde{g}_{12,n} x_2 + h_{12,n})$									
	Formula		Formula		Formula		Formula		
$\tilde{\tau}_{1,n}$	$-b_{12} + 2\tilde{\beta}_{1,n}^2 \tau_{a,1}$	$\tilde{u}_{12,n}$	$\frac{2\pi^2 \tilde{\beta}_{1,n}^2 + i\pi d_{12} \tilde{\tau}_{1,n}}{b_{12} \tilde{\tau}_{1,n}}$	$\tilde{v}_{a,12,n}$	$\frac{i2\pi}{\tilde{\tau}_{1,n}}$	$\tilde{h}_{a,12,n}$	$-\frac{b_{12} g_{01}}{\sqrt{\tilde{\tau}_{1,n}} \sqrt{\tilde{\Gamma}_{1,n}}}$	$\tilde{\theta}_{12,n}$	$\frac{b_{12} u_{01} + i\pi a_{12}}{\tilde{\tau}_{1,n}}$
$\tilde{\chi}_{a,12,n}$	$\sqrt{2\pi} \sqrt{\frac{i\tilde{\beta}_{1,n}^2}{\tilde{\tau}_{1,n}}} \left(\frac{\tilde{\Gamma}_{1,n}}{\tilde{\tau}_{1,n}} \right)^{1/2}$	$\tilde{g}_{12,n}$	$\frac{2i\pi \tilde{\beta}_{1,n}^2 g_{01}}{\sqrt{\tilde{\tau}_{1,n}} \sqrt{\tilde{\Gamma}_{1,n}}}$	$v_{12,n}$	$\tilde{v}_{a,12,n} x_{1,n}$	$h_{12,n}$	$\tilde{h}_{a,12,n} x_{1,n}$	$\chi_{12,n}$	$\tilde{\chi}_{a,12,n} e^{-\tilde{\theta}_{12,n} x_{1,n}^2}$
$\Psi_{j+1,n}(x_{j+1}) = \chi_{01} \left(\prod_{i=1}^j \chi_{i,i+1,n} \right) \exp(\tilde{u}_{j,j+1,n} x_{j+1}^2 + v_{j,j+1,n} x_{j+1}) H_l(\tilde{g}_{j,j+1,n} x_{j+1} + h_{j,j+1,n})$ for $j \in [2, N-1]$									
	Formula		Formula		Formula		Formula		
$\tilde{\tau}_{j,n}$	$-b_{j,j+1} + 2\tilde{\beta}_{j,n}^2 \tilde{\tau}_{a,j,n}$	$\tilde{u}_{j,j+1,n}$	$\frac{2\pi^2 \tilde{\beta}_{j,n}^2 + i\pi d_{j,j+1} \tilde{\tau}_{j,n}}{b_{j,j+1} \tilde{\tau}_{j,n}}$	$\tilde{v}_{a,j,j+1,n}$	$\frac{i2\pi}{\tilde{\tau}_{j,n}}$	$\tilde{\Gamma}_{j,n}$		$2\tilde{\beta}_{j,n}^2 b_{j,j+1} \tilde{g}_{j-1,j,n}^2 + \tilde{\tau}_{j,n}$	
$\tilde{\theta}_{a,j,j+1,n}$	$-\frac{\tilde{\beta}_{j,n}^2 b_{j,j+1}}{2\tilde{\tau}_{j,n}}$	$\tilde{\theta}_{b,j,j+1,n}$	$-\frac{b_{j,j+1}}{\tilde{\tau}_{j,n}}$	$\tilde{\theta}_{c,j,j+1,n}$	$-\frac{b_{j,j+1} \tilde{u}_{j-1,j,n} + i\pi a_{j,j+1}}{\tilde{\tau}_{j,n}}$	$\tilde{h}_{c,j,j+1,n}$	$-\frac{\tilde{\beta}_{j,n}^2 b_{j,j+1} \tilde{g}_{j-1,j,n}}{\sqrt{\tilde{\tau}_{j,n}} \sqrt{\tilde{\Gamma}_{j,n}}}$		
$\tilde{h}_{a,j,j+1,n}$	$\frac{\sqrt{\tilde{\tau}_{j,n}}}{\sqrt{\tilde{\Gamma}_{j,n}}}$	$\tilde{h}_{b,j,j+1,n}$	$-\frac{b_{j,j+1} \tilde{g}_{j-1,j,n}}{\sqrt{\tilde{\tau}_{j,n}} \sqrt{\tilde{\Gamma}_{j,n}}}$	$\tilde{\chi}_{a,j,j+1,n}$	$\sqrt{2\pi} \sqrt{-\frac{\tilde{\beta}_{j,n}^2}{\tilde{\tau}_{j,n}}} \left(\frac{\tilde{\Gamma}_{j,n}}{\tilde{\tau}_{j,n}} \right)^{1/2}$	$\tilde{g}_{j,j+1,n}$	$\frac{2i\pi \tilde{\beta}_{j,n}^2 \tilde{g}_{j-1,j,n}}{\sqrt{\tilde{\tau}_{j,n}} \sqrt{\tilde{\Gamma}_{j,n}}}$		
$h_{j,j+1,n}$	$h_{j-1,j,n} \tilde{h}_{a,j,j+1,n} + \tilde{h}_{b,j,j+1,n} x_{j,n} + v_{j-1,j,n} \tilde{h}_{c,j,j+1,n}$	$v_{j,j+1,n}$	$\tilde{v}_{a,j,j+1,n} \times (x_{j,n} + \tilde{\beta}_{j,n}^2 v_{j-1,j,n})$	$\chi_{j,j+1,n}$	$\tilde{\chi}_{a,j,j+1,n} \exp(v_{j-1,j,n} \tilde{\theta}_{b,j,j+1,n} x_{j,n} + \tilde{\theta}_{c,j,j+1,n} x_{j,n}^2 + v_{j-1,j,n}^2 \tilde{\theta}_{a,j,j+1,n} - \frac{i\pi}{4})$				

- [22] J. C. Lagarias, "The computational complexity of simultaneous Diophantine approximation problems," *SIAM Journal on Computing*, vol. 14, no. 1, pp. 196–209, 1985.
- [23] J. W. Goodman, *Introduction to Fourier Optics*, Colorado, USA: Roberts & Company Publishers, 2005.
- [24] R. P. Feynman, A. R. Hibbs and D. F. Styer, *Quantum Mechanics and Path Integrals*, emended ed, New York, USA: Dover Publications, Jul. 2010.
- [25] A. Erdélyi and H. Bateman, *Tables of Integral Transforms, vol. II.*, McGraw-Hill, 1954.
- [26] E. W. Weisstein, "Hermite polynomial," 2002. [Online] Available: <http://mathworld.wolfram.com/HermitePolynomial.html>
- [27] J. Wen and M. Breazeale, "A diffraction beam field expressed as the superposition of Gaussian beams," *The Journal of the Acoustical Society of America*, vol. 83, no. 5, pp. 1752–1756, 1988.
- [28] D. Ding and X. Liu, "Approximate description for Bessel, Bessel–Gauss, and Gaussian beams with finite aperture," *JOSA A*, vol. 16, no. 6, pp. 1286–1293, 1999.
- [29] X. Lu, C. Wei, L. Liu, G. Wu, F. Wang and Y. Cai, "Experimental study of the fractional Fourier transform for a hollow Gaussian beam," *Optics & Laser Technology*, vol. 56, pp. 92–98, 2014.
- [30] I. G. daPaz, C. H. S. Vieira, R. Ducharme, L. A. Cabral, H. Alexander and M. D. R. Sampaio, "Gouy phase in nonclassical

paths in a triple-slit interference experiment," *Phys. Rev. A*, vol. 93, no. 3, p. 033621, Mar. 2016.